

Simulation program and application analysis of nuclear magnetic resonance gyroscope signal considering Rb-Xe coupling

Jia-Jia Li(李佳佳), Yi Zhang(张燚), Zhi-Guo Wang(汪之国), Qi-Yuan Jiang(江奇渊), Yong-Hui Liang(梁永辉), Yi-Cheng Deng(邓意成), Bing-Feng Sun(孙兵锋), Tian-Shun Wang(王天顺)

Citation: Chin. Phys. B. 35, 094204 (2026). DOI: 10.1088/1674-1056/ae1deb |
CSTR: 32038.14.CPB.ae1deb
http://cpb.iphy.ac.cn; http://iopscience.iop.org/cpb

What follows is a list of articles you may be interested in

Response analysis of NMRG system considering Rb–Xe coupling

Yi Zhang(张燚), Qiyuan Jiang(江奇渊), Bingfeng Sun(孙兵锋), Jiahu Wei(魏加湖), Lin Yang(杨麟), Yongyuan Li(李永远), Zhiguo Wang(汪之国), Kaiyong Yang(杨开勇), Hui Luo(罗晖)
Chin. Phys. B. 33, 094203 (2024). DOI: 10.1088/1674-1056/ad6130

Simple and robust method for rapid cooling of ^{87}Rb to quantum degeneracy

Chun-Hua Wei(魏春华), Shu-Hua Yan(颜树华)
Chin. Phys. B. 29, 064208 (2020). DOI: 10.1088/1674-1056/ab8625

Laser frequency offset-locking using electromagnetically induced transparency spectroscopy of ^{85}Rb in magnetic field

Han-Mu Wang(王汉睦), Hong Cheng(成红), Shan-Shan Zhang(张珊珊), Pei-Pei Xin(辛培培), Zi-Shan Xu(徐子珊), Hong-Ping Liu(刘红平)
Chin. Phys. B. 27, 094205 (2018). DOI: 10.1088/1674-1056/27/9/094205

High quality electromagnetically induced transparency spectroscopy of ^{87}Rb in a buffer gas cell with a magnetic field

Hong Cheng(成红), Han-Mu Wang(王汉睦), Shan-Shan Zhang(张珊珊), Pei-Pei Xin(辛培培), Jun Luo(罗军), Hong-Ping Liu(刘红平)
Chin. Phys. B. 26, 074204 (2017). DOI: 10.1088/1674-1056/26/7/074204

Investigation of the nonlinear CPT spectrum of ^{87}Rb and its application for large dynamic magnetic measurement

Chi Xu(徐迟), Shi-Guang Wang(王时光), Yong Hu(胡勇), Yan-Ying Feng(冯焱颖), Li-Jun Wang(王力军)
Chin. Phys. B. 26, 064203 (2017). DOI: 10.1088/1674-1056/26/6/064203

Simulation program and application analysis of nuclear magnetic resonance gyroscope signal considering Rb–Xe coupling

Jia-Jia Li(李佳佳)[1,2,3], Yi Zhang(张燚)[1,2,3], Zhi-Guo Wang(汪之国)[1,2,3], Qi-Yuan Jiang(江奇渊)[1,2,3], Yong-Hui Liang(梁永辉)[1,2,3], Yi-Cheng Deng(邓意成)[4,5], Bing-Feng Sun(孙兵锋)[1,2,3,†], and Tian-Shun Wang(王天顺)[4,5,‡]

[1] *College of Advanced Interdisciplinary Studies, National University of Defense Technology, Changsha* 410073, *China*
[2] *Hunan Key Laboratory of Mechanism and Technology of Quantum Information, National University of Defense Technology, Changsha* 410073, *China*
[3] *Nanhu Laser Laboratory, National University of Defense Technology, Changsha* 410073, *China*
[4] *Beijing Institute of Aerospace Control Devices, Beijing* 100854, *China*
[5] *Quantum Engineering Research Center of the CASC, Beijing* 100094, *China*

(Received 8 September 2025; revised manuscript received 30 October 2025; accepted manuscript online 11 November 2025)

The nuclear magnetic resonance gyroscope (NMRG) holds significant promise for applications in unmanned systems, smart devices, and deep-sea/space exploration. However, its advancement is constrained by multiphysical interference and coupling effects. Current techniques lack the capability for high-precision multi-axis decoupling or accurate mechanistic analysis of performance-limiting factors, restricting further enhancements in accuracy. To overcome this, we developed a signal simulation program incorporating critical NMRG physical effects, Rb–Xe coupling, carrier demodulation, and phase-locked loop (PLL) feedback control, using a fourth-order Runge–Kutta numerical solver. The model was validated through dual verification via main magnetic field variations and closed-loop PLL phase shifts, achieving an error margin below 0.2%. Using this platform, we systematically evaluated the impact of magnetic field parameters on key performance metrics: signal amplitude, resonance frequency, signal-to-noise ratio (SNR), and 100-second standard deviation. Key findings include: (i) Signal intensity and SNR display distinct trends under varying field parameters, likely due to field-dependent noise modulation; (ii) PLL excitation amplitude and phase exert the strongest influence on the 100-second deviation ($\sim 0.015°$/h), followed by high-frequency carrier excitation amplitude, with other parameters contributing under 0.005°/h; (iii) Optimizing the 100-second deviation requires leveraging the synergy between signal intensity and SNR. This simulation tool offers dual utility: guiding quantitative parameter optimization and system debugging in practical applications of NMRG, and visualizing the evolution of Rb and Xe atomic moments under varying fields, thereby improving mechanistic insight into NMRG operation.

Keywords: nuclear magnetic resonance gyroscope (NMRG), Rb–Xe coupling, signal simulation, error analysis

PACS: 42.81.Pa, 42.79.–e, 74.25.nj, 82.56.–b

DOI: 10.1088/1674-1056/ae1deb **CSTR:** 32038.14.CPB.ae1deb

1. Introduction

The NMRG, as a quantum inertial sensor, measures rotational motion by detecting shifts in the Larmor precession frequency of noble gas nuclear spins (*e.g.*, ^{129}Xe). Its advantages, including solid-state design (no moving parts), high shock resistance, acceleration insensitivity, and miniaturization capability, make it promising for high-precision navigation and attitude control. Consequently, it has become an active research focus in inertial technology. To meet the growing demand for navigation accuracy, substantial efforts have been devoted to enhancing its core performance through studies of physical mechanisms, noise suppression, and system optimization.[1–3]

Despite significant progress, the development of NMRGs continues to face critical challenges. A primary issue in analyzing their performance is the system's susceptibility to multiple coupled parameters, including optical fields,[4–6] thermal fluctuations,[7] and magnetic fields.[8] The strong interdependencies among these factors complicate the accurate isolation of each one's effect on the gyroscope. Previous studies have outlined key parameters (*e.g.*, pump laser power and frequency stability) necessary to achieve a bias stability of 0.01°/h[9] although attaining the target values for some parameters remains difficult under typical laboratory conditions. It has also been reported that magnetic fields and temperature can cause significant signal drift in NMRGs, which cannot be fully compensated for even using a dual-isotope scheme.[10] Comprehensive research in Ref. [11] examines the impact of the direct current (DC) magnetic field, modulation field frequency/phase, and Rb resonance linewidth on the phase stability, demonstrating notable improvement in drift stability us-

†Corresponding author. E-mail: sbf3375038@163.com
‡Corresponding author. E-mail: skyustc@163.com

© 2026 Chinese Physical Society and IOP Publishing Ltd. All rights, including for text and data mining, AI training, and similar technologies, are reserved.

ing a self-calibrating Rb parameter magnetometer. Our recent study[12,13] further demonstrated that the Rb–Xe coupling effect complicates the influence of control parameters (*e.g.*, magnetic field amplitude and frequency) on the NMRG signal. However, these studies have not yet incorporated the effects of practical control components such as filters and PLLs, meaning the behavior of an actual NMRG system is significantly more complex.

The magnetic field is essential for quantum state manipulation in NMRGs, and its configuration, particularly the orthogonality of the control fields, is a critical factor determining performance. However, calibration and compensation methods for non-orthogonal magnetic fields have received limited attention. Current research has predominantly focused on magnetic coil design,[14–17] magnetic compensation schemes,[18–20] and frequency shifts induced by field inhomogeneity.[21] By contrast, the specific influence of field configuration, especially non-orthogonality, on key performance metrics such as the SNR and 100-second standard deviation remains less explored.

Moreover, current simulation studies primarily concentrate on numerical solutions and noise characterization, but have paid little attention to the three-dimensional (3D) trajectory visualization of magnetic moments. For example, Jia *et al.* used COMSOL Multiphysics® to investigate the distributions of electron and nuclear spin polarizations in NMRG, but did not explore the intuitive visualization of dynamic magnetic moment evolution. The lack of such trajectory modeling hinders a deeper understanding of nutational motion and polarization relaxation phenomena, thereby limiting the utility of simulation data in exploring underlying mechanisms.[22]

This study presents a comprehensive NMRG signal simulation program that incorporates effects such as Rb–Xe coupling, carrier demodulation, and PLL feedback control. Using this program, the influence of magnetic field parameters on key performance metrics, including gyro signal amplitude, resonance frequency, SNR, and 100-second standard deviation, was systematically investigated. The results provide practical insights for NMRG system debugging and parameter optimization. Furthermore, the program enables visualization of magnetic moment evolution trajectories, offering an intuitive reference for analyzing the operational mechanism of the gyroscope.

2. Theoretical model

Current mainstream NMRG implementations begin by polarizing both Rb and Xe magnetic moments along the z-axis using a circularly polarized pump beam. A sequence of magnetic fields is then applied: first, the primary field B_0 along the z-axis, followed by the carrier field $B_c\cos(\omega_c t)$. Here, B_c and $\omega_c = 2\pi f_{B_c}$ are the amplitude and angular frequency of the carrier field, respectively, and f_{B_c} is the frequency. The PLL provides feedback by generating an x-axis excitation field that is precisely synchronized with the Xe precession. Concurrently, an Rb atomic magnetometer, constructed using the primary and modulation fields, measures the precession signals in the xy-plane. Finally, a linearly polarized probe beam, directed along the x-axis, is used to monitor the polarization rotation induced by variations in the Rb magnetometer's signal. This allows the Xe precession signal to be extracted for carrier rotation analysis. A schematic diagram of the working principle is shown in Fig. 1.

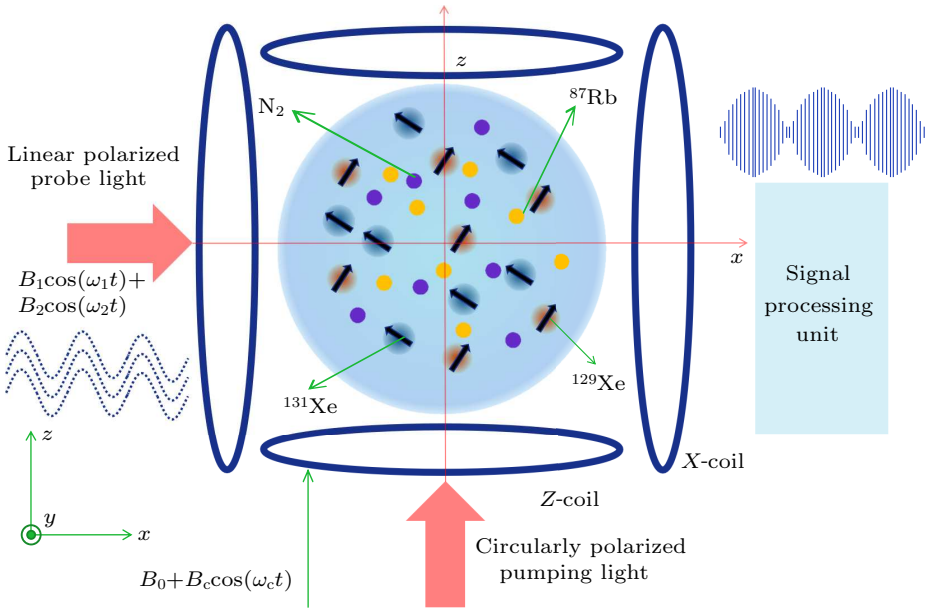


Fig. 1. Structure of NMRG.

However, in NMRG systems incorporating Rb–Xe coupling, the polarization dynamics of Rb and Xe atoms exhibit signif-

icant complexity. This necessitates the establishment of coupled differential equations to characterize the specific evolution of their polarization rates.

Based on Bloch approximation theory, the polarization rates of Rb and Xe atoms in an NMRG obey the following kinetic equations:[23]

$$\begin{aligned}
\frac{\mathrm{d}\boldsymbol{P}^{\mathrm{e}}}{\mathrm{d}t} &= \left\{ -\left[\frac{\gamma_{\mathrm{e}}}{Q(\boldsymbol{P}^{\mathrm{e}})}\left(\boldsymbol{B}+\lambda M_0^{\mathrm{n1}}\boldsymbol{P}^{\mathrm{n1}}+\lambda M_0^{\mathrm{n2}}\boldsymbol{P}^{\mathrm{n2}}+\boldsymbol{L}+\boldsymbol{\beta}^{\mathrm{e}}\right)+\boldsymbol{\Omega}\right]\times\boldsymbol{P}^{\mathrm{e}}\right. \\
&\quad \left. +\frac{R_{\mathrm{p}}\left(\boldsymbol{s}_{\mathrm{p}}-\boldsymbol{P}^{\mathrm{e}}\right)+R_{\mathrm{m}}\left(\boldsymbol{s}_{\mathrm{m}}-\boldsymbol{P}^{\mathrm{e}}\right)+R_{\mathrm{se}}^{\mathrm{en1}}\left(\boldsymbol{P}^{\mathrm{n1}}-\boldsymbol{P}^{\mathrm{e}}\right)+R_{\mathrm{se}}^{\mathrm{en2}}\left(\boldsymbol{P}^{\mathrm{n2}}-\boldsymbol{P}^{\mathrm{e}}\right)-R_{\mathrm{rest}}^{\mathrm{e}}\boldsymbol{P}^{\mathrm{e}}}{Q(\boldsymbol{P}^{\mathrm{e}})}\right\}, \\
\frac{\mathrm{d}\boldsymbol{P}^{\mathrm{n1}}}{\mathrm{d}t} &= -\left[\gamma_{\mathrm{n1}}\left(\boldsymbol{B}+\lambda M_0^{\mathrm{e}}\boldsymbol{P}^{\mathrm{e}}+\lambda M_0^{\mathrm{n2}}\boldsymbol{P}^{\mathrm{n2}}+\boldsymbol{\beta}^{\mathrm{n}}\right)+\boldsymbol{\Omega}\right]\times\boldsymbol{P}^{\mathrm{n1}}+R_{\mathrm{se}}^{\mathrm{n1e}}\left(\boldsymbol{P}^{\mathrm{e}}-\boldsymbol{P}^{\mathrm{n1}}\right)+R_{\mathrm{se}}^{\mathrm{n1n2}}\left(\boldsymbol{P}^{\mathrm{n2}}-\boldsymbol{P}^{\mathrm{n1}}\right)-R_{\mathrm{rest}}^{\mathrm{n1}}\boldsymbol{P}^{\mathrm{n1}}, \\
\frac{\mathrm{d}\boldsymbol{P}^{\mathrm{n2}}}{\mathrm{d}t} &= -\left[\gamma_{\mathrm{n2}}\left(\boldsymbol{B}+\lambda M_0^{\mathrm{e}}\boldsymbol{P}^{\mathrm{e}}+\lambda M_0^{\mathrm{n1}}\boldsymbol{P}^{\mathrm{n1}}+\boldsymbol{\beta}^{\mathrm{n}}\right)+\boldsymbol{\Omega}\right]\times\boldsymbol{P}^{\mathrm{n2}}+R_{\mathrm{se}}^{\mathrm{n2e}}\left(\boldsymbol{P}^{\mathrm{e}}-\boldsymbol{P}^{\mathrm{n2}}\right)+R_{\mathrm{se}}^{\mathrm{n2n1}}\left(\boldsymbol{P}^{\mathrm{n1}}-\boldsymbol{P}^{\mathrm{n2}}\right)-R_{\mathrm{rest}}^{\mathrm{n2}}\boldsymbol{P}^{\mathrm{n2}}. \qquad (1)
\end{aligned}$$

Here, $\boldsymbol{P}^{\mathrm{e}}$ represents the electron spin polarization vector of Rb atoms. $\boldsymbol{P}^{\mathrm{n1}}$ and $\boldsymbol{P}^{\mathrm{n2}}$ denote the spin polarization vectors of ^{129}Xe and ^{131}Xe nuclei, $\gamma_{\mathrm{e}}=\pm\mu_{\mathrm{S}}g_{\mathrm{S}}/\hbar$ and $\gamma_{\mathrm{n1,2}}=-\mu_{\mathrm{N}}g_{\mathrm{I}}/\hbar$ respectively indicate the gyromagnetic ratios of Rb electron spin and Xe nucleus spin relative to their respective nuclear spins. $Q(\boldsymbol{P}^{\mathrm{e}})$ represents the polarization-dependent slowing factor. $\boldsymbol{B}=\boldsymbol{B}_x+\boldsymbol{B}_y+\boldsymbol{B}_z$ denotes the external magnetic field vector, and $\boldsymbol{B}_x$, $\boldsymbol{B}_y$, and $\boldsymbol{B}_z$ represent the magnetic field components on x-axis, y-axis, and z-axis. $\boldsymbol{B}_z=B_0+B_{\mathrm{c}}\cos(\omega_{\mathrm{c}}t)$, $\boldsymbol{B}_x=B_1\cos(\omega_1 t)+B_2\cos(\omega_2 t)$, B_1, B_2, ω_1, and ω_2 are the strengths and angular frequencies of ^{129}Xe and ^{131}Xe. The relationship between polarization and magnetization is expressed as: $\boldsymbol{M}^{\mathrm{e}}=M_0^{\mathrm{e}}\boldsymbol{P}^{\mathrm{e}}$, $\boldsymbol{M}^{\mathrm{n1,2}}=M_0^{\mathrm{n1,2}}\boldsymbol{P}^{\mathrm{n1,2}}$, where M_0^{e} and $M_0^{\mathrm{n1,2}}$ represent the maximum magnetization intensities of electrons and nuclei respectively. $\lambda=8\pi\kappa_0/3$ contains a spin exchange enhancement factor κ_0 that accounts for spin–orbital coupling effects, while $\boldsymbol{L}$ represents the virtual magnetic field originating from the optical frequency shift AC–Stark effect. $\boldsymbol{\beta}^{\mathrm{e}}$ and $\boldsymbol{\beta}^{\mathrm{n}}$ represent other interactions coupled with electrons and nuclei respectively. $\boldsymbol{\Omega}$ denotes the rotational angular velocity of the carrier. R_{p} and R_{m} respectively denote the pump efficiency of pump light and probe light. $\boldsymbol{s}_{\mathrm{p}}$ and $\boldsymbol{s}_{\mathrm{m}}$ represent the photon spin vectors of pump light and probe light respectively. $R_{\mathrm{se}}^{\mathrm{en}}$ and $R_{\mathrm{se}}^{\mathrm{ne}}$ indicate the exchange polarization rates between electron spin and nuclear spin, while $R_{\mathrm{rest}}^{\mathrm{e}}$ and $R_{\mathrm{rest}}^{\mathrm{n}}$ represent the relaxation rates of other mechanisms involving electron and nuclear spins. Using $\gamma_{\mathrm{Rb}}=\gamma_{\mathrm{e}}/Q(\boldsymbol{P}^{\mathrm{e}})$, with the main magnetic field direction the z-axis, and setting

$$\begin{aligned}
\tau_2 &= \frac{Q}{R_{\mathrm{p}}+R_{\mathrm{m}}+R_{\mathrm{se}}^{\mathrm{en1}}+R_{\mathrm{se}}^{\mathrm{en2}}+R_{\mathrm{rest},x/y}^{\mathrm{e}}}, \\
\tau_1 &= \frac{Q}{R_{\mathrm{p}}+R_{\mathrm{m}}+R_{\mathrm{se}}^{\mathrm{en1}}+R_{\mathrm{se}}^{\mathrm{en2}}+R_{\mathrm{rest},z}^{\mathrm{e}}}, \\
P_{x/y}^{\mathrm{e0}} &= \frac{R_{\mathrm{p}}s_{x/y}^{p}+R_{\mathrm{m}}s_{x/y}^{m}+R_{\mathrm{se}}^{\mathrm{en1}}P_{x/y}^{\mathrm{n1}}+R_{\mathrm{se}}^{\mathrm{en2}}P_{x/y}^{\mathrm{n2}}}{R_{\mathrm{p}}+R_{\mathrm{m}}+R_{\mathrm{se}}^{\mathrm{en1}}+R_{\mathrm{se}}^{\mathrm{en2}}+R_{\mathrm{rest},x/y}^{\mathrm{e}}}, \\
P_z^{\mathrm{e0}} &= \frac{R_{\mathrm{p}}s_z^{p}+R_{\mathrm{m}}s_z^{m}+R_{\mathrm{se}}^{\mathrm{en1}}P_z^{\mathrm{n1}}+R_{\mathrm{se}}^{\mathrm{en2}}P_z^{\mathrm{n2}}}{R_{\mathrm{p}}+R_{\mathrm{m}}+R_{\mathrm{se}}^{\mathrm{en1}}+R_{\mathrm{se}}^{\mathrm{en2}}+R_{\mathrm{rest},z}^{\mathrm{e}}}, \\
T_2^{\mathrm{n1/2}} &= \frac{1}{R_{\mathrm{se}}^{\mathrm{n1/2e}}+R_{\mathrm{se}}^{\mathrm{n1/2n2/1}}+R_{\mathrm{rest},x/y}^{\mathrm{n1/2}}}, \\
T_1^{\mathrm{n1/2}} &= \frac{1}{R_{\mathrm{se}}^{\mathrm{n1/2e}}+R_{\mathrm{se}}^{\mathrm{n1/2n2/1}}+R_{\mathrm{rest},z}^{\mathrm{n1/2}}}, \\
P_{x/y}^{\mathrm{n1/20}} &= \frac{R_{\mathrm{se}}^{\mathrm{n1/2e}}P_{x/y}^{\mathrm{e}}+R_{\mathrm{se}}^{\mathrm{n1/2n2/1}}P_{x/y}^{\mathrm{n2/1}}}{R_{\mathrm{se}}^{\mathrm{n1/2e}}+R_{\mathrm{se}}^{\mathrm{n1/2n2/1}}+R_{\mathrm{rest},x/y}^{\mathrm{n1/2}}}, \\
P_z^{\mathrm{n1/20}} &= \frac{R_{\mathrm{se}}^{\mathrm{n1/2e}}P_z^{\mathrm{e}}+R_{\mathrm{se}}^{\mathrm{n1/2n2/1}}P_z^{\mathrm{n2/1}}}{R_{\mathrm{se}}^{\mathrm{n1/2e}}+R_{\mathrm{se}}^{\mathrm{n1/2n2/1}}+R_{\mathrm{rest},z}^{\mathrm{n1/2}}}, \\
\boldsymbol{B}^{\mathrm{e}} &= \boldsymbol{B}+\boldsymbol{L}+\boldsymbol{\beta}^{\boldsymbol{e}}+\boldsymbol{\Omega}/\gamma_{\mathrm{Rb}}+\lambda M_0^{\mathrm{n1}}\boldsymbol{P}^{\mathrm{n1}}+\lambda M_0^{\mathrm{n2}}\boldsymbol{P}^{\mathrm{n2}}, \\
\boldsymbol{B}^{\mathrm{n1}} &= \boldsymbol{B}+\boldsymbol{\beta}^{\mathrm{n1}}+\boldsymbol{\Omega}/\gamma_{\mathrm{n1}}+\lambda M_0^{\mathrm{e}}\boldsymbol{P}^{\mathrm{e}}+\lambda M_0^{\mathrm{n2}}\boldsymbol{P}^{\mathrm{n2}}, \\
\boldsymbol{B}^{\mathrm{n2}} &= \boldsymbol{B}+\boldsymbol{\beta}^{\mathrm{n2}}+\boldsymbol{\Omega}/\gamma_{\mathrm{n2}}+\lambda M_0^{\mathrm{e}}\boldsymbol{P}^{\mathrm{e}}+\lambda M_0^{\mathrm{n1}}\boldsymbol{P}^{\mathrm{n1}}. \qquad (2)
\end{aligned}$$

Express Eq. (1) in Cartesian coordinates and simplify to derive the standard Bloch equation

$$\begin{aligned}
\frac{\mathrm{d}P_x^{\mathrm{e}}}{\mathrm{d}t} &= -\gamma_{\mathrm{Rb}}\left(B_y^{\mathrm{e}}P_z^{\mathrm{e}}-B_z^{\mathrm{e}}P_y^{\mathrm{e}}\right)+\frac{P_x^{\mathrm{e0}}-P_x^{\mathrm{e}}}{\tau_2}, \\
\frac{\mathrm{d}P_y^{\mathrm{e}}}{\mathrm{d}t} &= -\gamma_{\mathrm{Rb}}\left(B_z^{\mathrm{e}}P_x^{\mathrm{e}}-B_x^{\mathrm{e}}P_z^{\mathrm{e}}\right)+\frac{P_y^{\mathrm{e0}}-P_y^{\mathrm{e}}}{\tau_2}, \\
\frac{\mathrm{d}P_z^{\mathrm{e}}}{\mathrm{d}t} &= -\gamma_{\mathrm{Rb}}\left(B_x^{\mathrm{e}}P_y^{\mathrm{e}}-B_y^{\mathrm{e}}P_x^{\mathrm{e}}\right)+\frac{P_z^{\mathrm{e0}}-P_z^{\mathrm{e}}}{\tau_1}, \\
\frac{\mathrm{d}P_x^{\mathrm{n1}}}{\mathrm{d}t} &= -\gamma_{\mathrm{n1}}\left(B_y^{\mathrm{n1}}P_z^{\mathrm{n1}}-B_z^{\mathrm{n1}}P_y^{\mathrm{n1}}\right)+\frac{P_x^{\mathrm{n10}}-P_x^{\mathrm{n1}}}{T_2^{\mathrm{n1}}}, \\
\frac{\mathrm{d}P_y^{\mathrm{n1}}}{\mathrm{d}t} &= -\gamma_{\mathrm{n1}}\left(B_z^{\mathrm{n1}}P_x^{\mathrm{n1}}-B_x^{\mathrm{n1}}P_z^{\mathrm{n1}}\right)+\frac{P_y^{\mathrm{n10}}-P_y^{\mathrm{n1}}}{T_2^{\mathrm{n1}}}, \\
\frac{\mathrm{d}P_z^{\mathrm{n1}}}{\mathrm{d}t} &= -\gamma_{\mathrm{n1}}\left(B_x^{\mathrm{n1}}P_y^{\mathrm{n1}}-B_y^{\mathrm{n1}}P_x^{\mathrm{n1}}\right)+\frac{P_z^{\mathrm{n10}}-P_z^{\mathrm{n1}}}{T_1^{\mathrm{n1}}}, \\
\frac{\mathrm{d}P_x^{\mathrm{n2}}}{\mathrm{d}t} &= -\gamma_{\mathrm{n2}}\left(B_y^{\mathrm{n2}}P_z^{\mathrm{n2}}-B_z^{\mathrm{n2}}P_y^{\mathrm{n2}}\right)+\frac{P_x^{\mathrm{n20}}-P_x^{\mathrm{n2}}}{T_2^{\mathrm{n2}}}, \\
\frac{\mathrm{d}P_y^{\mathrm{n2}}}{\mathrm{d}t} &= -\gamma_{\mathrm{n2}}\left(B_z^{\mathrm{n2}}P_x^{\mathrm{n2}}-B_x^{\mathrm{n2}}P_z^{\mathrm{n2}}\right)+\frac{P_y^{\mathrm{n20}}-P_y^{\mathrm{n2}}}{T_2^{\mathrm{n2}}},
\end{aligned}$$

$$\frac{\mathrm{d}P_z^{\mathrm{n}2}}{\mathrm{d}t} = -\gamma_{\mathrm{n}2}\left(B_x^{\mathrm{n}2}P_y^{\mathrm{n}2} - B_y^{\mathrm{n}2}P_x^{\mathrm{n}2}\right) + \frac{P_z^{\mathrm{n}20} - P_z^{\mathrm{n}2}}{T_1^{\mathrm{n}2}}. \quad (3)$$

3. Simulation and experimental verification

3.1. NMRG simulation program

To implement the established NMRG theoretical model and develop a simulation program for analyzing how varying magnetic field parameters affect the gyro signals, we first numerically solve the Bloch equation (3) that describes the triatomic coupling in NMRG. The parameters for these equations are defined in Eq. (2). We employ the fourth-order Runge–Kutta method to obtain the numerical solution

$$\begin{aligned}
&y' = f(t,y),\\
&y_{\mathrm{n}+1} = y_{\mathrm{n}} + \frac{h}{6}(k_1 + 2k_2 + 2k_3 + k_4),\\
&k_1 = f(t_{\mathrm{n}}, y_{\mathrm{n}}),\\
&k_2 = f(t_{\mathrm{n}} + h/2, y_{\mathrm{n}} + k_1 h/2),\\
&k_3 = f(t_{\mathrm{n}} + h/2, y_{\mathrm{n}} + k_2 h/2),\\
&k_4 = f(t_{\mathrm{n}} + h, y_{\mathrm{n}} + k_3 h).
\end{aligned} \quad (4)$$

Here, $y' = f(t,y)$ is the differential equation to be solved numerically, $y_{\mathrm{n}+1} = y_{\mathrm{n}} + \frac{h}{6}(k_1 + 2k_2 + 2k_3 + k_4)$ is the iteration formula for discretization of the differential equation. t_{n} and y_{n} are the known values of the independent variable and the dependent variable in the n-th step, respectively. k_1, k_2, k_3, and k_4 are four slope approximate values corresponding to different stages, k_1 stands for the slope at the starting point of the calculation interval, k_2 and k_3 refer to the two corrected slopes at the interval midpoint, and k_4 represents the slope at the ending point. $h = x_{\mathrm{n}+1} - x_{\mathrm{n}}$ is the step size of the numerical calculation interval, n represents the number of time discretization steps. For the multiple coupling equations given in Eq. (3), the specific fourth-order Runge–Kutta equations can be written as

$$\begin{aligned}
&P_i' = f_i\left(t, \{P_j\}\right),\\
&P_{i,n+1} = P_{i,n} + \frac{h}{6}(k_{i,1} + 2k_{i,2} + 2k_{i,3} + k_{i,4}),\\
&k_{i,1} = f_i\left(t_{\mathrm{n}}, \{P_{j,n}\}\right),\\
&k_{i,2} = f_i\left(t_{\mathrm{n}} + h/2, \{P_{j,n} + k_{j,1}h/2\}\right),\\
&k_{i,3} = f_i\left(t_{\mathrm{n}} + h/2, \{P_{j,n} + k_{j,2}h/2\}\right),\\
&k_{i,4} = f_i\left(t_{\mathrm{n}} + h, \{P_{j,n} + k_{j,3}h\}\right).
\end{aligned} \quad (5)$$

Here, $i, j = 1, \ldots, 9$ represent 9 different polarization rate components in Eq. (3), P' represents the derivative of the polarization rate component in Eq. (3), that is, the amount that changes with time. The above is the specific process of solving the coupling equations of three atomic polarization rates in the NMRG using the fourth-order Runge–Kutta method.

In the numerical implementation, the characteristic frequencies of Rb and Xe atoms and the computational efficiency are considered. To address this, within each computation cycle, the six polarization equations for the Xe atoms in Eq. (3) are solved first, followed by recalculating the three equations for the Rb atoms. This sequence mirrors the physical process of the NMRG: the rotational response is primarily sensed by the Xe atoms, and the resulting change in the Xe magnetic moment is then detected via the Rb atoms. To enhance computational efficiency, the coupled system of nine differential equations is decoupled into three independent sets according to atomic species, with their interactions incorporated through an effective magnetic field. This approach significantly increases the calculation speed while preserving the essential physics, thereby ensuring the reliability of the results. The detailed program flowchart is shown in Fig. 2.

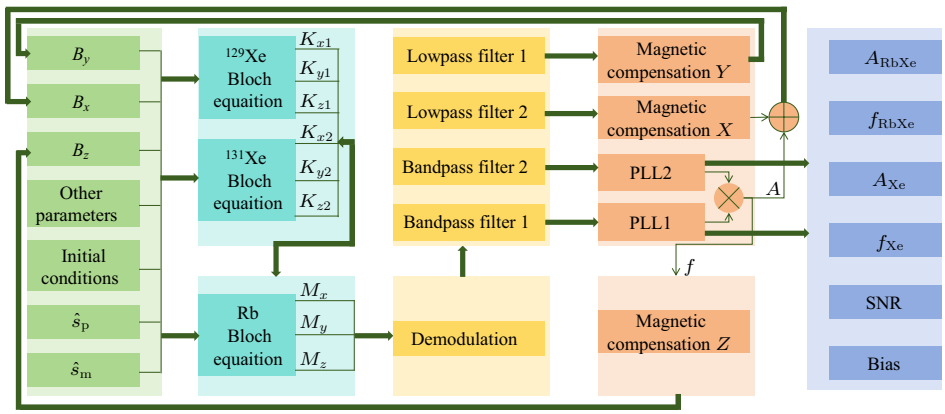


Fig. 2. Flow chart of NMRG simulation program. Where A is the excitation amplitude of PLL applied to X-axis, and f is the resonant frequency obtained by PLL.

Other parameters include nonmagnetic field parameters such as various relaxation rates and rotation-related parameters in Eq. (1). The initial conditions are the parameters when the system reaches a steady-state equilibrium operating state. $\hat{s}_{\mathrm{p}}$ and $\hat{s}_{\mathrm{m}}$ respectively represent the pump light and the probe light. K_{x1}, K_{y1}, and K_{z1} are the components of the magnetic moment of ^{129}Xe on the three axes, while K_{x2}, K_{y2}, and K_{z2} are the components of the magnetic moment of ^{131}Xe, while

M_x, M_y, and M_z are the components of the magnetic moment of ^{87}Rb.

The NMRG signal simulation program developed in this study is built on a computational framework comprising four key components: parameter input, numerical solution, signal processing, and feedback control. The specific steps are as follows:

Step 1 Parameter input and initialization (green module in Fig. 2): The simulation is initialized with a complete set of core parameters and initial conditions derived from the experimental system. These parameters, which include control magnetic fields, relaxation rates, and pump/probe light properties, provide the foundational input for the simulation.

Step 2 Numerical solution of the Rb–Xe coupled Bloch equations (cyan module in Fig. 2). The input parameters are used to define the Rb–Xe coupled Bloch equations, which are then solved numerically using the fourth-order Runge–Kutta method (see Eq. (5)). The double-headed arrow between the Rb and Xe in the figure illustrates their mutual coupling: Rb polarizes the Xe atoms via spin-exchange optical pumping, while also serving as the medium for detecting the resulting Xe magnetic moment.

Step 3 Signal preprocessing and bidirectional feedback (yellow module, Fig. 2): The raw magnetic moment signals from the Bloch equation solutions are first preprocessed in this module. Key steps include demodulation, low-pass filtering, and band-pass filtering to remove noise and extract the effective signals. This yields two main signal paths: one provides the residual magnetic fields along the x- and y-axes, while the other sends the processed signal to the orange module for final extraction of the Xe precession signal via dual PLLs.

Step 4 Feedback control and output (orange and purple modules, Fig. 2): This stage implements real-time, closed-loop control and generates the final outputs. PID control compensates for the x- and y-axis residual fields. The Xe precession signal from the PLLs serves three critical purposes: (i) It is fed back as the x-axis excitation field to the Bloch equations (green module), maintaining a stable Xe precession. (ii) The phase difference between a PLL and a reference signal acts as an error input to another PID controller. This controller generates a compensation signal for the z-axis coil, stabilizing the main magnetic field against fluctuations. (iii) Another portion is sent to the purple module for detailed analysis, producing the core NMRG performance metrics, such as signal frequency, amplitude, SNR, and the 100-second standard deviation.

In summary, parameter transfer and closed-loop feedback across these modules enable a full-link simulation of the NMRG signal, from input parameters to characteristic output.

3.2. Comparison of simulation and experimental results

To validate the simulation program, the experimental setup shown in Fig. 3 was constructed. It consists of the following key subsystems.

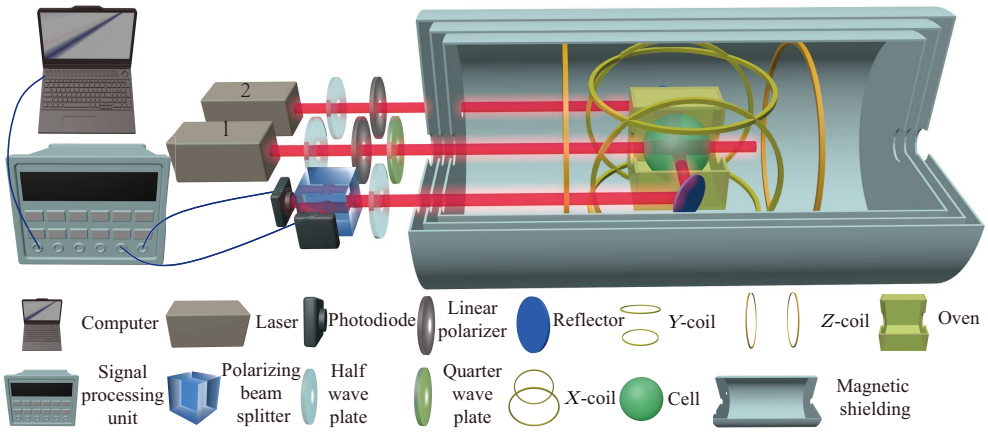


Fig. 3. Experimental setup.

(i) A magnetic shielding system isolates external magnetic interference, providing a stable, low-noise magnetic environment for the core sensor.

(ii) A triaxial magnetic coil system for generating controllable static and alternating magnetic fields along three orthogonal directions.

(iii) A non-magnetic heating system for regulating the temperature of the atomic vapor cell.

(iv) The core atomic vapor cell contains the working media: ^{87}Rb, ^{129}Xe, ^{131}Xe isotopes, and N_2 buffer gas.

(v) An optical pumping path based on a 795-nm semiconductor (laser 1). The emitted linearly polarized light is converted into circularly polarized light via a combination of a half-wave plate, a linear polarizer, and a quarter-wave plate. This provides adjustable-power pump light for polarizing the ^{87}Rb atoms.

(vi) An optical probe path employing a 780-nm semiconductor (laser 2). The output is a linearly polarized beam whose

polarization angle can be adjusted by a half-wave plate and a linear polarizer. After passing through the vapor cell, the probe beam, which now carries polarization rotation information, is split by a second half-wave plate and a polarizing beam splitter. The two resulting beams are detected by a balanced photodetector for noise suppression.

(vii) A signal processing unit that integrates lock-in amplifiers, data acquisition (DAQ) cards, control circuitry, and a computer for parameter measurement, system control, and data analysis.

Experimental parameter optimization: The system parameters were first optimized experimentally. A static magnetic field of 12.155 μT was applied along the z-axis, along with a high-frequency carrier field at an optimized frequency of 85,074 Hz. The demodulation phase of the magnetometer was adjusted to make it sensitive to the y-component of the field. Using these optimized ^{87}Rb parameters, an alternating current (AC) magnetic field was then applied along the x-axis. The amplitude and phase of the ^{129}Xe PLL excitation were adjusted to maximize its response signal near resonance, yielding a real-time precession frequency fluctuating around 144.206 Hz.

Simulation parameters: The simulation parameters were chosen to match the experimental conditions, as summarized in Table 1. The main magnetic field B_0 was set to 12.155 μT, f_{B_c} was set to 85074 Hz, and B_c was maintained at 16 μT, consistent with the experimental system. The ^{129}Xe PLL excitation amplitude was −1 nT. To mimic realistic conditions, Gaussian white noise with a standard deviation of 10 pT was added to the z-axis magnetic field. This configuration, with a consistent noise sequence across all simulations, allows for a precise analysis of the effects of individual parameter variations under identical stochastic conditions.

Table 1. Simulation parameters of NMRG.

Parameter	Value	Unit	Parameter	Value	Unit
λM_0^{n1e}, λM_0^{n2e}	0.01	V	R_{se}^{n1e}	0.01	s^{-1}
λM_0^{en1}, λM_0^{en2}	1	V	R_{se}^{n1n2}	0.0001	s^{-1}
λM_0^{n1n2}, λM_0^{n2n1}	0.0001	V	$R_{rest,x}^{n1}$	0.01	s^{-1}
R_p	10000	s^{-1}	$R_{rest,y}^{n1}$	0.01	s^{-1}
R_m	100	s^{-1}	$R_{rest,z}^{n1}$	0.001	s^{-1}
R_{se}^{en1}	0.01	s^{-1}	R_{se}^{n2e}	0.001	s^{-1}
R_{se}^{en2}	0.01	s^{-1}	R_{se}^{n2n1}	0.0001	s^{-1}
$R_{rest,x}^{e}$	30000	s^{-1}	$R_{rest,x}^{n2}$	0.04	s^{-1}
$R_{rest,y}^{e}$	30000	s^{-1}	$R_{rest,y}^{n2}$	0.04	s^{-1}
$R_{rest,z}^{e}$	10000	s^{-1}	$R_{rest,z}^{n2}$	0.01	s^{-1}
γ_{Rb}	2Pi*(–6998)	rad/s/μT	γ_{n1}	2Pi*(–11.86)	rad/s/μT
γ_{n2}	2Pi*(3.516)	rad/s/μT	Q	4.7	
B_0	12.155	μT	B_1	–0.001	μT
B_c	16	μT	f_{B_c}	85074	Hz

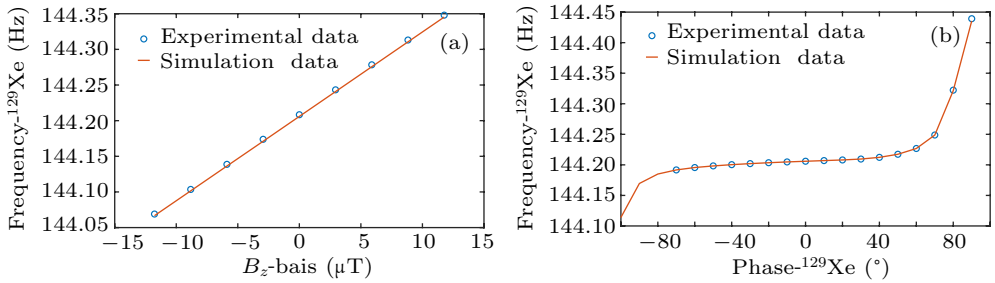


Fig. 4. Comparison of precession frequency variations between simulation system and experimental system. Panel (a) shows the variation of the precession frequency of ^{129}Xe obtained by experiment (blue) and simulation (red) when the static magnetic field of the main axis changes. Panel (b) shows the variation of precession frequency of ^{129}Xe obtained by simulation and experiment when the phase of the PLL of ^{129}Xe changes.

To validate the simulation program, we conducted two comparative experiments using the aforementioned system and parameters.

First, the z-axis magnetic field (B_z) was varied while other conditions were held constant in both the experimental and simulation systems. Figure 4(a) shows the resulting variation in the closed-loop resonance frequency of ^{129}Xe. The frequency increases with B_z in both cases, and the simulation results agree well with the experimental data, with a maximum error of less than 0.2%.

Second, the phase deviation between the PLL excitation signal and the Xe precession signal was adjusted, again while keeping other parameters constant. The relationship between the ^{129}Xe resonance frequency and this phase deviation is detailed in Fig. 4(b). As in the first experiment, the frequency increases with the phase deviation, and the simulation matches

the experiment within 0.2% error. Conversely, unlike the linear response to B_z, a distinct nonlinear relationship is observed when adjusting the phase.

The close agreement in both experiments confirms the effectiveness of our simulation program for NMRG signal analysis. The following section uses this validated program to analyze the influence of different magnetic field parameters on the NMRG's performance.

4. Analysis of simulation results

Based on the experimentally validated simulation program, this study systematically analyzes the variation patterns of key parameters, including the Xe atom polarization amplitude A_{Xe}, ^{129}Xe resonance frequency F_{req}, the amplitude A_{RbXe} of Xe atomic magnetic moment measured by the Rb atomic magnetometer embedded in NMRG, SNR, and the gyroscope bias drift Bias. The Bias was calculated using the 100-second standard deviation after one hour of stable operation with the single isotope ^{129}Xe (total duration of 4300 seconds, excluding the initial 700 seconds of unstable data). The specific research variables are as follows:

(i) The embedded Rb magnetometer parameters. The carrier magnetic field of the embedded Rb magnetometer is a critical adjustable parameter. Although its influence has been extensively studied theoretically in standalone magnetometers,[24] analyses considering the Rb–Xe coupling within an NMRG are relatively scarce, despite being unavoidable during NMRG debugging. The influence of the embedded Rb magnetometer is modeled by an expression $B_{\mathrm{c}}\cos(2\pi f_{B_{\mathrm{c}}}+\theta)$ involving three key parameters: carrier magnetic field frequency $f_{B_{\mathrm{c}}}$, amplitude B_{c}, and demodulation phase θ. Simulations were performed by varying these parameters around their adjusted baseline values. The tested ranges were ±0.3 kHz, ±4 μT, and $\pm20°$, with step sizes of 0.15 kHz, 2 μT, and 10° respectively. The x-axis coordinates in the results represent the deviations from the baseline: $\delta f_{B_{\mathrm{c}}}$, δB_{c}, $\delta\theta$.

(ii) Parameters of the ^{129}Xe PLL. The closed-loop feedback excitation magnetic field $B_1\cos(2\pi f_1+\alpha)$ applied along the x-direction is crucial for maintaining the stable precession of Xe magnetic moments. The amplitude B_1 and phase deviation α are also key parameters in NMRG debugging. However, research on their influence on NMRG performance, especially on long-term stability metrics like the 100-second standard deviation, remains limited. The influence of these parameters is studied by varying B_1 from -3 nT to -0.5 nT in steps of 0.5 nT. For α, the simulations were conducted around the optimal value (set as the central 0 point) within a range of $\pm20°$ and a step size of 10°. The marked horizontal coordinate represents the phase difference $\delta\alpha$.

(iii) Axial static magnetic field bias. The axial bias magnetic field is defined by two components: the deviation δB_0 of the main axis magnetic field B_0 from its set value, and the residual magnetic field δB_x along the x-axis. During simulations, these two parameters were varied around their central values (specified in Table 1) within a range of ±20 nT, using a uniform step size of 10 nT.

(iv) Non-orthogonal inter-axis angles. Practical machining and assembly tolerances in NMRG construction often lead to non-orthogonality among the magnetic field coils, an issue noted in several studies that have proposed various calibration methods.[18,19] However, the specific impact of coil misalignment on NMRG performance has received comparatively less attention. The present analysis can also provide useful insights for the machining tolerance specifications of the field coils. To model the magnetic field generated by non-orthogonal coils, a gyroscope coordinate system is defined as follows: the z-axis is aligned with the pump light direction, the x-axis with the probe light direction, and the y-axis is perpendicular to the xz-plane, coinciding with the nominal direction of the y-axis coil field. Let B'_z, B'_x, and B'_y represent the magnetic fields intended to be generated by the z-, x-, and y-axis coils, respectively. When the z-axis and x-axis coils are misaligned by spatial angles θ_z and θ_x relative to the gyroscope coordinate system, the components of the resulting magnetic field in the gyroscope system can be calculated using Eq. (6), as illustrated in Fig. 5.

$$\begin{aligned} B_x &= B'_x\cos\theta_x + B'_z\sin\theta_z\cos\varphi_z,\\ B_y &= B'_x\sin\theta_x\sin\varphi_x + B'_z\sin\theta_z\sin\varphi_z + B'_y,\\ B_z &= B'_x\sin\theta_x\cos\varphi_x + B'_z\cos\theta_z. \end{aligned} \tag{6}$$

Here, φ_x is the azimuthal angle between the x-axis and the projection of magnetic field B'_x onto the xy-plane, while angle φ_z represents the polar angle between the z-axis and the projection of field B'_z onto the yz-plane. The non-orthogonal magnetic field consists of an x-axis non-orthogonal angle $\delta\theta_x$ and a z-axis non-orthogonal angle $\delta\theta_z$, both ranging from $-20°$ to $+20°$ with a uniform step size of 10°.

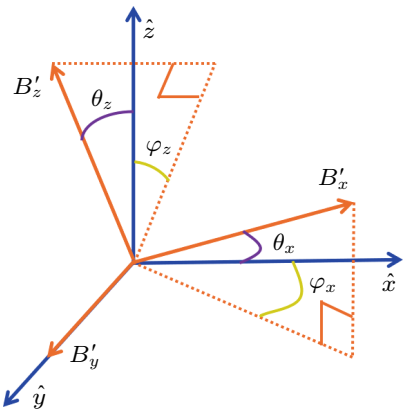


Fig. 5. Definition of orthogonal coordinate system for NMRG.

4.1. The influence of different magnetic field parameters on F_{req}

Simulations were performed for the different magnetic field parameters described above. The resulting variations of F_{req} obtained are presented in Fig. 6.

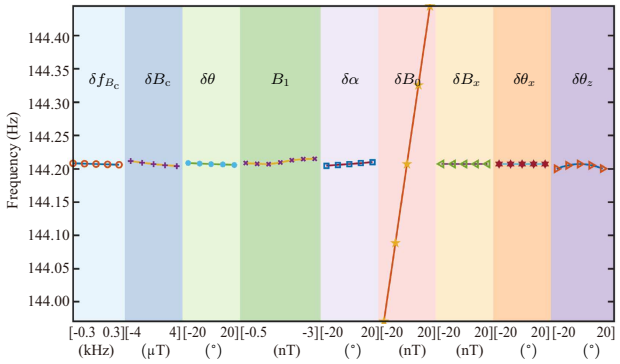


Fig. 6. The influence of all magnetic field parameters on F_{req}.

From left to right, it sequentially presents the variation of F_{req} with the individual changes of 9 physical quantities, including f_{B_c}, B_c, θ, B_1, α, δB_0, δB_0, $\delta\theta_x$, and $\delta\theta_z$. The abscissa of each grid provides the variation range value of the corresponding physical quantity, and the second row shows the corresponding unit. The δf_{B_c} is ± 0.3 kHz, δB_c is ± 4 μT, $\delta\theta$, $\delta\alpha$, $\delta\theta_x$, and $\delta\theta_z$ are all $\pm 20°$, B_1 ranges from -0.5 nT to -3 nT, δB_0 and δB_x are both ± 20 nT based on the data in Table 1.

We define the relative influence amplitude as $\delta_1 = 10^3 \times (F_{\mathrm{req_{max}}} - F_{\mathrm{req_{min}}})$, and detailed results are presented in Table 2.

Table 2. The peak-to-peak values of each parameter on F_{req}.

Parameters	f_{B_c}	B_c	θ	B_1	α	δB_0	δB_x	$\delta\theta_x$	$\delta\theta_z$
δ_1 (mHz)	2.17	7.36	2.81	7.98	5.50	473.58	0.14	0.03	7.04

The simulation results in Fig. 6 reveal that F_{req} increases linearly with δB_0, which is its most significant influencing parameter. This linear relationship is consistent with the fundamental principle of NMR, $f = \gamma B_0/(2\pi)$, and underscores the critical importance of magnetic field stability for NMRG performance. The last two columns respectively present the influence of $\delta\theta_x$ and $\delta\theta_z$, which arise from manufacturing and assembly errors, on the gyroscope's output. The comparison reveals that $\delta\theta_z$ has a more pronounced effect than $\delta\theta_x$. This is because $\delta\theta_z$ causes the magnetic field intended for the z-axis to have a projected component in the transverse plane, effectively reducing its magnitude along the z-axis. Consequently, F_{req} decreases for all non-zero $\delta\theta_z$ values, exhibiting a symmetric response about $\delta\theta_z$ of 0°. It is important to note that during operation, temperature variations can induce thermal deformation of the coil structure, altering $\delta\theta_z$ and leading to signal drift. Therefore, the coil design must account for thermal stability and structural symmetry to mitigate this effect.

The 4th and 5th columns present the influences of B_1 and $\delta\alpha$ of PLL output on F_{req}. According to the notation in Ref. [12], the phase difference between α and β is related to the magnetometer's state parameters, α contains the phase delay of various filter components and the artificially added phase deviation when the PLL generates the transverse magnetic field signal and β is the phase difference between the Xe precession signal and the PLL feedback signal. Therefore, without changing other parameters of the system, adjusting α has a similar effect to adjusting β. The influence of β on F_{req} has been provided in Ref. [10], as shown in the second equation in Eq. (7).[10,12] While the influence of B_1 on F_{req} is not given in Eq. (7). In fact, our research shows that the influence mechanism of B_1 on F_{req} is more complex, mainly because B_1 affects K_z, and K_z in turn affects the z-direction magnetic field sensed by the Rb magnetometer, which then influences $\arctan(B/A)$.

$$\begin{aligned} K_\perp &= \frac{\gamma^{\mathrm{Xe}} B_1 \cos\beta}{2\Gamma_2} K_z, \\ \dot{\phi} &= \omega_z - \Gamma_2 \tan\beta, \\ K_z &= \frac{K_0}{1 + \frac{\left(\gamma^{\mathrm{Xe}} B_1 \cos\beta\right)^2}{4\Gamma_1\Gamma_2}}, \end{aligned} \tag{7}$$

where $K_\perp$ is the sum vector of K_x and K_y.

Finally, parameters related to the Rb magnetometer, such as f_{B_c}, B_c, and θ, all affect F_{req} through the Rb–Xe coupling effect. For a detailed analysis, please refer to Ref. [12].

4.2. The influence of different magnetic field parameters on A_{Xe}

Simulations were carried out under the above different magnetic field parameters, and the changes in A_{Xe} obtained are shown in Fig. 7.

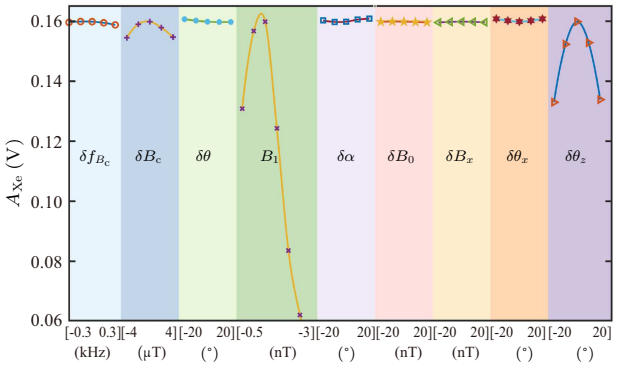


Fig. 7. The influence of all magnetic field parameters same with Fig. 6 on A_{Xe}.

We define the relative influence amplitude as $\delta_2 = 100\% * (A_{\mathrm{Xe-max}} - A_{\mathrm{Xe-min}})/A_{\mathrm{Xe-max}}$, and detailed results are presented in Table 3.

Table 3. The peak-to-peak values of each parameter on A_{Xe}.

Parameters	f_{B_c}	B_c	θ	B_1	α	δB_0	δB_x	$\delta\theta_x$	$\delta\theta_z$
$\delta_2/\%$	0.70	3.37	0.59	69.02	0.66	0.16	0.16	0.59	16.80

It can be observed from the figure that, unlike in Fig. 6 where B_0 has the most significant impact on F_{req}, B_1 exerts the most prominent influence on A_{Xe} under different conditions. Additionally, there exists a specific amplitude of B_1 where A_{Xe} reaches a maximum. This phenomenon can also be explained using the closed-loop given in Eq. (7). By substituting the third equation in Eq. (7) into the first one and performing differentiation, B_1 corresponding to the maximum A_{Xe} can be derived as $B_1 = \pm\frac{2\sqrt{\Gamma_1\Gamma_2}}{\gamma^{\text{Xe}}\cos\beta}$. In addition to B_1, $\delta\theta_z$ of the z-direction magnetic field coil also exerts a relatively significant influence on A_{Xe}. Similar to its influence on F_{req}, this effect also exhibits symmetry with respect to zero tilt. As is known, $\delta\theta_z$ reduces the magnetic field component along the z-axis while introducing an additional magnetic field component in the x-direction. However, from the 6th and 7th columns in Fig. 7, it is observed that δB_x has an insignificant impact on A_{Xe}. This observation leads to the inference that the influence on A_{Xe} at this point may mainly come from the tilt of B_{c}. This conclusion is consistent with the phenomenon shown in the 2nd column of the figure, where variations in the carrier magnetic field amplitude B_{c} also have a relatively significant effect on A_{Xe}. Finally, to intuitively illustrate the influence of magnetic field parameters on the precession of the Xe magnetic moment, our simulation program can also directly plot the precession trajectory of the Xe magnetic moment under different magnetic field parameters. As shown in Fig. 8, the influences of different B_1 and different $\delta\theta_z$ on the precession trajectory of the Xe magnetic moment are presented respectively.

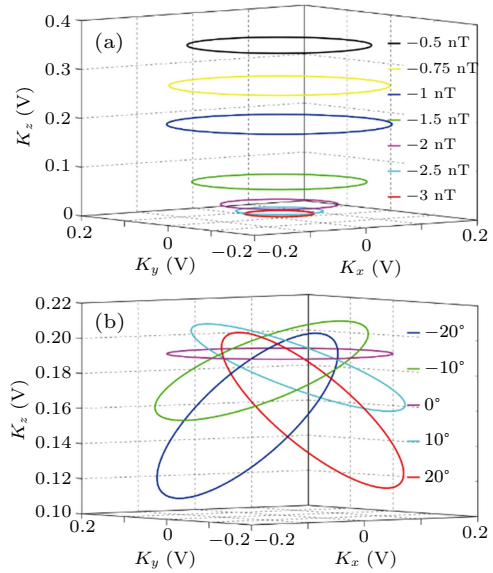


Fig. 8. The precession trajectory of the Xe magnetic moment under different B_1 and $\delta\theta_z$. (a) Precession trajectory of the Xe magnetic moment under different B_1. (b) Precession trajectory of the Xe magnetic moment under different $\delta\theta_z$.

As shown in Fig. 8(a), as the amplitude of B_1 increases, K_z progressively decreases. In contrast, both K_x and K_y initially increase to a maximum before decreasing. This characteristic behavior can be explained by the system's response described in Eq. (7). From Fig. 8(b), it is evident that as $\delta\theta_z$ increases, the center of K_z gradually decreases. The projection of the evolutionary trajectory onto the xy plane transforms from circular to elliptical as the z-axis tilts toward the x-axis, leading to a deviation of the vector from the original z-direction. This occurs because the tilt deviates the total magnetic field vector away from the original z-direction. The resulting elliptical transformation is symmetric with respect to both positive and negative tilt angles.

4.3. The influence of different magnetic field parameters on A_{RbXe}

Above, we have analyzed the effects of 9 different magnetic field parameters on F_{req} and A_{Xe} of the Xe magnetic moment precession signal in NMRG. However, in NMRG, the precession magnetic moment cannot be directly measured; instead, the Xe magnetic moment precession signal is indirectly acquired through an embedded alkali metal magnetometer such as Rb. Consequently, the signal actually measured by the NMRG is influenced by magnetic field parameters in a way that differs from their inherent effects on the Xe precession itself. This difference arises because these parameters also alter the operating state of the Rb magnetometer, thereby influencing its measurement results.

To more directly characterize the impact of these 9 magnetic field parameters on the output signal characteristics of the NMRG, we further investigated their effects on the Rb magnetometer's output signal. Our research reveals that A_{RbXe}measured by the Rb magnetometer varies significantly with these parameters, as shown in Fig. 9.

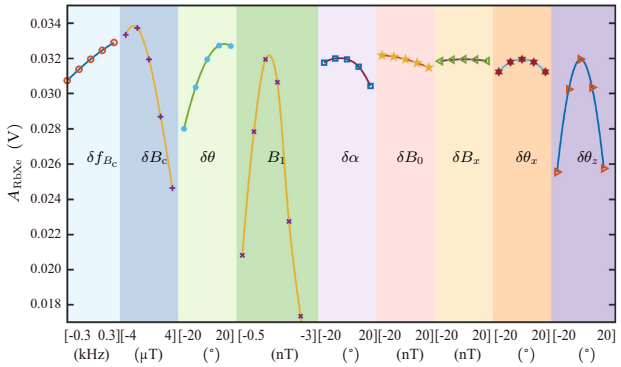


Fig. 9. The influence of all magnetic field parameters on A_{RbXe} under the same parameters with Fig. 6.

We define the relative influence amplitude as $\delta_3 = 100\% * (A_{\text{RbXe-max}} - A_{\text{RbXe-min}})/A_{\text{RbXe-max}}$; detailed results are presented in Table 4.

Table 4. The peak-to- peak values of each parameter on A_{RbXe}.

Parameters	f_{B_c}	B_c	θ	B_1	α	δB_0	δB_x	$\delta\theta_x$	$\delta\theta_z$
$\delta_3/\%$	6.56	26.95	14.47	56.29	4.88	2.14	0.34	2.23	20.03

First, similar to the trend shown in Fig. 7, both B_1 and $\delta\theta_z$ significantly affect the A_{RbXe}. For B_1, its peak influence consistently occurs at the third data point during the sweep, while the effect of $\delta\theta_z$ remains symmetric around zero. However, the relative influence amplitude has shifted when compared to the direct measurement case. For instance, the contribution of B_1 decreased from 69.02% to 56.29%, whereas the relative influence amplitude of $\delta\theta_z$ increased from 16.8% to 20.03%. Crucially, unlike magnetometer parameters such as B_c that affect the precession of the Xe magnetic moment through the Rb–Xe coupling effect, these magnetometer parameters can act directly on the signal of the Rb magnetometer. Consequently, the influence of magnetometer parameters like B_c on the Xe magnetic moment precession signal measured by the Rb magnetometer has been significantly enhanced. For instance, the relative influence amplitude of B_c increased from 3.37% (on the amplitude of the Xe's own precession signal) to 26.95%, representing an amplification of nearly an order of magnitude. The effects of other directly-acting parameters are also amplified to varying degrees. These findings demonstrate that the embedded Rb magnetometer, while essential for detection, introduces additional sensitivity to its own state parameters, thereby increasing the system's susceptibility to instability. Consequently, maintaining the magnetometer's stable operation is paramount for enhancing NMRG performance. This challenge is addressed in Ref. [11], which proposes effective strategies for stabilizing the Rb magnetometer.

4.4. The influence of different magnetic field parameters on SNR

To directly link the influences of the 9 magnetic field parameters to NMRG performance, we applied a white noise base with an amplitude of 10 pT in the z-direction. The SNR was calculated by comparing the root mean square (RMS) amplitude of the signal averaged over 100 s to the RMS amplitude of the noise within a 10-Hz bandwidth centered at 150 Hz. The specific setup is shown in Fig. 10. To ensure consistent influence of random noise across all tests, the same white noise random sequence was used throughout the testing process for each magnetic field parameter.

We define the relative influence amplitude as $\delta_4 = 100\% * (\mathrm{SNR}_{\max} - \mathrm{SNR}_{\min})/\mathrm{SNR}_{\max}$; detailed results are presented in Table 5.

Table 5. The peak-to- peak values of each parameter on SNR.

Parameters	f_{B_c}	B_c	θ	B_1	α	δB_0	δB_x	$\delta\theta_x$	$\delta\theta_z$
δ_4/%	25.83	35.12	31.73	51.65	37.88	55.95	4.53	6.12	30.37

The variation of SNR with the 9 magnetic field parameters exhibits a significant discrepancy compared to the variation in Fig. 9. This discrepancy likely stems from the frequency-dependent response characteristics of the Rb magnetometer to noise. As elaborated in Ref. [20], the response of the Rb–Xe coupling system to the z-direction magnetic field is highly sensitive to various system parameters, and changes in the 9 parameters under study may alter these noise-response characteristics. A critical observation from Fig. 10 and Fig. 9 is that maximizing the NMRG signal amplitude by adjusting parameters like B_1 does not necessarily yield the maximum SNR. In some cases, a relatively high SNR can be achieved even when B_1 is very small. This highlights the necessity of considering both signal amplitude and SNR comprehensively during NMRG parameter debugging. More notably, the influence of certain parameters (*e.g.*, f_{B_c}, θ) on A_{RbXe} and SNR can be diametrically opposed. For instance, data from the first column of the figure indicate that A_{RbXe} increases monotonically with the increase of f_{B_c}, while the SNR decreases monotonically with the increase of f_{B_c}. This opposing trend suggests that the mechanisms governing signal generation and noise susceptibility may involve different pathways within the coupled system. Furthermore, when noise is considered, the relative influence amplitude of some parameters on the SNR is substantially greater than that on A_{RbXe}. For example, the influence amplitude of δB_0 on A_{RbXe} is only 2.14%, whereas its influence on SNR is as high as 55.95%. This stark contrast underscores that NMRG debugging must not focus solely on maximizing the A_{RbXe} but requires a balanced optimization that accounts for SNR degradation. Finally, the influence of some parameters becomes more complex when noise is factored in. $\delta\theta_x$ and $\delta\theta_z$ may exhibit non-monotonic or interactive effects, necessitating more sophisticated tuning strategies.

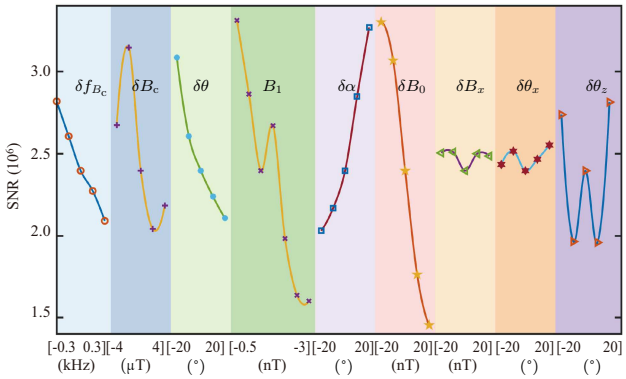


Fig. 10. The influence of all magnetic field parameters same with Fig. 6 on SNR.

4.5. The influence of different magnetic field parameters on V_{Bias}

In the current performance testing of NMRG, the 100-second standard deviation V_{Bias} is commonly used to quantify the stability of the gyroscope system. Therefore, under the same noise settings as those in the SNR diagram, we collected

3600 s of resonance frequency data for each set of configured magnetic field parameters after the signal reached a stable state. The V_{Bias} was then calculated based on this dataset, and the specific results are shown in Fig. 11.

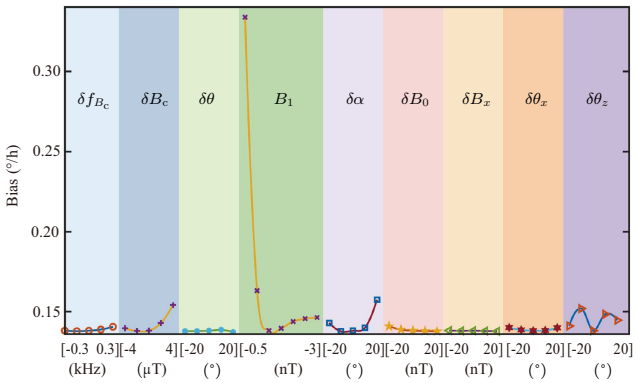


Fig. 11. The influence of all magnetic field parameters same with Fig. 6 on V_{Bias}.

We define the relative influence amplitude as $\delta_5 = 100\% * (b_{\max} - b_{\min})/b_{\max}$, and detailed results are presented in Table 6.

Table 6. The peak-to-peak values of each parameter on Bias.

Parameters	f_{B_c}	B_c	θ	B_1	α	δB_0	δB_x	$\delta\theta_x$	$\delta\theta_z$
$\delta_5/\%$	1.95	10.56	0.98	19.55	12.59	2.23	0.32	1.39	9.05

It can be observed that variations of B_1 have the most significant impact on V_{Bias} of NMRG, with δ_5 reaching 19.55%. A closer inspection reveals that the minimum V_{Bias} occurs at the third data point, where the measured signal amplitude is the largest, yet the SNR is not the maximum. In contrast, the first data point in the configuration yields the highest SNR but exhibits the largest V_{Bias}, indicating the poorest gyroscope stability at this operating condition. In addition, variations of α and B_c also exert relatively large impacts on the V_{Bias} of NMRG. By comparing with the previous signal amplitude and SNR diagrams, a stronger correlation is observed between V_{Bias} and the signal amplitude for these two parameters: a larger signal amplitude generally corresponds to a smaller V_{Bias}, and *vice versa*. Therefore, if the optimization objective is to minimize V_{Bias}, better results may be achieved by referring to the variation of signal amplitude when adjusting parameters such as B_1, α, and B_c. Finally, some parameters that have a significant impact on SNR exert only a minor influence on V_{Bias}, for example, the main magnetic field B_0. Moreover, compared with their influence on SNR, the influences of f_{B_c} and α on Bias are also significantly reduced. It is thus evident that different optimal parameter configurations may be required for different performance index requirements in NMRG, due to the trade-off between signal amplitude, SNR, and stability.

Among all parameters, B_1 demonstrates the most significant impact on A_{RbXe}, SNR, and V_{Bias}. Consequently, selecting optimal B_1 is crucial for achieving optimal V_{Bias}. PLL parameter α optimization proves equally critical. Our experimental data indicate that maximizing the signal amplitude A_{RbXe} measured by the Rb magnetometer (rather than pursuing peak SNR) during PLL adjustment yields superior stability. Although fluctuations in magnetometer parameters and axial residual magnetism within a small range near optimal values may affect A_{RbXe} and SNR, their impact on V_{Bias} remains relatively minor. The presence of inter-axis non-orthogonal angles, particularly those in the Z-axis spindle, exerts greater influence on A_{RbXe} and SNR, while its effect on Bias is less pronounced compared to PLL parameter adjustments.

5. Conclusion

This study establishes a dynamic model for NMRG that incorporates Rb–Xe coupling and non-orthogonal magnetic fields. A dynamic simulation platform utilizing a fourth-order Runge–Kutta algorithm was developed to visualize the spatial evolution of Xe magnetic moment under varying magnetic field parameters. The reliability of this NMRG signal simulation program, which accounts for Rb–Xe coupling, was verified through experimental comparisons. By implementing a consistent sequence of random magnetic field noise across different configurations, this research investigated the direct impacts of various magnetic field parameters on the gyroscope's A_{RbXe}, SNR, and bias drift. Numerical simulations under identical noise conditions enabled a quantitative analysis of the relative influence of each magnetic parameter. Within the simulated parameter variation range, the amplitude of the ^{129}Xe PLL excitation field B_1 exhibits the most significant impact on V_{Bias}, followed by its $\delta\alpha$. The influence of other parameters is considerably smaller. The demodulation phase $\delta\theta$ of the Rb magnetometer plays a decisive role in achieving a smaller value of V_{Bias}. This simulation program provides valuable guidance for the quantitative optimization of NMRG magnetic field parameters, serving as a reliable theoretical simulation tool for high-precision NMRG design. The findings from simulating magnetic field parameters establish a foundation for subsequent investigations into optical parameters and temperature control, offering practical insights for experimental research.

We will further study the case under the operation of double isotopic magnetic compensation later, but the situation will become more complicated due to the existence of ^{131}Xe electric quadrupole moment and the increase of coupling after adding parameters. In order to simplify and clarify the idea, we first study the case of a single isotope in this paper.

Acknowledgements

Project supported by the National Natural Science Foundation of China (Grant Nos. U23B2066 and 12174446), the Open-end fund (Grant No. WDZC20230201), the Science and Technology Innovation Program of Hunan Province, China (Grant No. 2025QK3010), and the Outstanding Youth Science Fund of Hunan Province, China (Grant No. 2023JJ10050).

References

[1] Eklund E J 2008 *Microgyroscope Based on Spin-Polarized Nuclei* (Ph.D. Dissertation) (Irvine: University of California, Irvine)
[2] Sorensen S S, Thrasher D A and Walker T G 2020 *Applied Sciences* **10** 7099
[3] Kornack T W, Ghosh R K and Romalis M V 2005 *Phys. Rev. Lett.* **95** 230801
[4] Zhuang M J, Fan X T, Wang T S and Liu Y X 2021 *Laser Journal* **42** 1
[5] Zhou W Y, Wang X F, Deng Y C and Liu Y X 2017 *Navigation and Control* **16** 47
[6] Huang W, Liu Y X, He Y, Wang Y and Huo L 2018 *Navigation and Control* **17** 33
[7] Okunevich A I and Dovator N A 2019 *J. Phys.: Conf. Ser.* **1400** 066034
[8] Liu Y, Pang H Y, Ma L Y, Quan J L, Fan W F, Wu Z H and Quan W 2023 *Measurement* **222** 113656
[9] Vershovskii A K, Litmanovich Yu A, Pazgalev A S and Peshekhonov V G 2018 *Gyroscopy Navig.* **9** 162
[10] Walker T G and Larsen M S 2016 *Adv. Atom. Mol. Opt. Phys.* **65** 373
[11] Gao G P, Hu J B, Tang F, Liu W H, Zhang X D, Wang B X, Deng D G, Zhu M Z and Zhao N 2024 *Phys. Rev. Appl.* **21** 014042
[12] Zhang Y, Li J J, Jiang Q Y, Wang Z G, Luo H and Yang K Y 2022 *Journal of Magnetic Resonance* **344** 107295
[13] Zhang Y, Jiang Q Y, Sun B F, Wei J H, Yang L, Li Y Y, Wang Z G, Yang K Y and Luo H 2024 *Chin. Phys. B* **33** 094203
[14] Hobson P J, Hardwicke N L, Davis A, Smith T X, Morley C, Packer M, Holmes N, Weil M A, Brookes M J, Bowtell R and Fromhold M 2023 *IEEE Trans. Instrum. Meas.* **72** 1
[15] Hobson P J, Holmes N, Patel P, Styles B, Chalmers J, Morley C, Davis A, Packer M, Smith T X, Raudonyte S, Holmes D, Harrison R, Woolger D, Sims D, Brookes M J, Bowtell R and Fromhold M 2023 *IEEE Trans. Instrum. Meas.* **72** 1
[16] Tayler M C D, Mouloudakis K, Zetter R, Hunter D, Lucivero V G, Bodenstedt S, Parkkonen L and Mitchell M W 2022 *Phys. Rev. Appl.* **18** 014036
[17] Han B C, Zhou W Y, Xu X P, Sun J J, Zhao F W, Jiang Q and Qin J S 2023 *IEEE Trans. Instrum. Meas.* **72** 1
[18] Li S R, Ma D Y, Lu J X, Xing B Z, Wang K, Gao Y N and Han B C 2022 *Measurement* **202** 111878
[19] Yang K, Lu J X, Ma Y N, Wang Z X, Sun B W, Wang Y G and Han B C 2022 *IEEE Trans. Instrum. Meas.* **71** 1
[20] Wang K, Ma D, Li S, Gao Y and Sun J 2023 *S Sensors and Actuators A: Physical* **349** 114055
[21] Zhang X D, Hu J B, Xiao D W and Zhao N 2025 *Commun. Phys.* **8** 93
[22] Jia Y C, Liu Z C, Zhou B Q, Liang X Y, Wu W F, Peng J P, Ding M, Zhai Y Y and Fang J C 2019 *J. Phys. D: Appl. Phys.* **52** 355001
[23] Liu F, Duan L, Fan W, Pang H, Liu S and Quan W 2022 *IEEE Sensors Journal* **22** 1990
[24] Shu Q, Ji F and Zhu M Z 2022 *Journal of Magnetic Resonance* **335** 107128